DOI: 10.13009/EUCASS2025-130
11TH EUROPEAN CONFERENCE FOR AERONAUTICS AND SPACE SCIENCES (EUCASS)

Experimental and Numerical Analysis of the Intermittentency in a Nozzle Overexpanded-Flow

Emanuele Martelli[⋆†], *Vincent Jaunet*[⋆⋆], *Giacomo della Posta*[††] *and Matteo Bernardini*[††]
[⋆]*Politecnico di Torino*
Corso Duca degli Abruzzi 24, 10129, Torino, Italia
[⋆⋆]*ISAE-ENSMA Institut PPRIME*
Avenue Clement Ader, 86360 Chasseneuil-du-Poitou, France
[††]*"Sapienza" University of Rome*
Via Eudossiana 18, 00184, Roma, Italia
emanuele.martelli@polito.it · vincent.jaunet@ensma.fr · giacomo.dellaposta@uniroma1.it · matteo.bernardini@uniroma1.it
[†]Corresponding author

Abstract
The present work reports an investigation into the statistical properties of wall-pressure fluctuations in a highly over-expanded nozzle flow, characterized by significant shock-induced flow separation. This regime is extremely hazardous in rocket nozzles, as it leads to very high off-axis loads. The database under investigation has been obtained both experimentally and numerically by means of a hybrid RANS/LES simulation of the flow issuing from a sub-scale Truncated Ideal Contour (TIC) nozzle, fed with cold air and operating at a Reynolds number on the order of 10^7. The degree of over-expansion is quantified by the nozzle pressure ratio (NPR). The experimental campaign was conducted in the S150 supersonic wind tunnel at the Institut PPRIME in Poitiers. Pressure fluctuations are extracted from several probes positioned along the nozzle wall, considering different NPR values. The intermittent behavior is investigated using conditional statistics based on the wavelet transform, which demonstrates that the aerodynamic loads of the over-expanded jet consist of intermittent bursts rather than continuous variations. The wavelet analysis reveals scale-by-scale intermittency and, in particular, shows that the wall-pressure signals exhibit a significant degree of intermittency around the frequency associated with aerodynamic side-loads. The statistics of these intermittent events, in terms of the time delay between occurrences, are found to be weakly sensitive to NPR and appear to follow a universal behavior that can be modeled by a log-normal distribution. This finding may support the development of a side-load behavior model incorporating the key features identified by the statistical analysis presented here.

1. Introduction

Supersonic nozzles that equip liquid rocket engines (LREs) of launchers' first stages experience internal flow separation during the ignition sequence, since they are necessarily over-expanded during this transient. Internal flow separation entails shock wave/boundary layer interaction (SBLI) and consequent thermal and fatigue loading, mainly due to off-axis side loads that intense enough to induce the structural failure of the nozzle.[17] Depending on the nozzle contour and on the nozzle pressure ratio, defined as the ratio between the inlet total pressure and the ambient pressure, $NPR = p_0/p_a$, two different kinds of shock-induced flow separation can appear: free shock separation (FSS) and restricted shock separation.[17] Earlier investigations considered the problem by developing analytical and empirical tools capable of describing the occurrence of side loads, originating by the FSS state, the RSS state or by the transition from one configuration to another.[8,18] All of these methods were mainly intended for use as design tools.

As both numerical and experimental disciplines have made numerous advances in the last decades, efforts have recently shifted towards a more physical understanding of the mechanisms responsible for off-axis forces in over-expanded nozzles with internal flow-separation. The experimental work of Baars et al.[1] on a parabolic nozzle was one of the first to conduct a Fourier-azimuthal decomposition of the unsteady wall-pressure field, revealing how the breathing zeroth mode is characterized by most of the total resolved pressure-fluctuation energy, whereas the side-load inducing first azimuthal mode has less than half of the total energy. Later, the experimental work of Jaunet et al.[10] on a truncated ideal contour (TIC) nozzle, confirmed that the low-frequency shock motion is mainly linked to the axisymmetric azimuthal mode, whereas the middle-frequency peaks, identified in the spectral analysis, are shown to

DOI: 10.13009/EUCASS2025-130

be very organized in the azimuthal direction, each one of them clearly associated with a preferred azimuthal mode. At NPR=9, the strongest peak is entirely contained in the first azimuthal mode, which is the only mode that can contribute to the off-axis loads. The authors have also shown that this tonal dynamics was not due to transonic resonance,[14] but it was not yet clear whether it could be attributed to a screech-like mechanism since it did not radiate tonal sound, although its frequency scaled nicely with the screech frequency model prediction.[10] Martelli et al.[16] conducted one of the first delayed detached eddy simulation (DDES) on a similar nozzle, and they confirmed the presence of a coherent azimuthal anti-symmetric mode. In their work, the authors also proposed a model for a screech-like resonance, consisting of a closed feedback loop. The forward path involves the shedding of vorticity from the triple point of the Mach disk toward the second Mach disk in the plume, while the backward path involves the subsonic recirculation region between the nozzle-wall and the detached supersonic shear layer. For the backward path, Bakulu et al.[2] instead proposed one of the guided jet modes,[20] whereas Morisco et al.[21] again indicated the subsonic recirculation region. Jaunet and Lehsnasch[11] have recently shown that a supersonic over-expanded jet, such as the one exiting a TIC nozzle, is an excellent support for a variety of guided jet modes that could close the feedback loop. Nevertheless, since no frequency prediction and detailed observation of these modes is available, the exact nature of the feedback loop in this case still remains an open question and deserves further investigation. One aspect on which there seems to be agreement, instead, is that the entire jet column is subject to instabilities and unsteadiness, observable in various azimuthal modes frequencies, and a particular characteristic of this unsteady behaviour is its intermittent nature. In the work of Camussi et al.[5] and Kearney et al.[13] it is found that both the external field and the nozzle-wall pressure signature emanating from a compressible jet are characterized indeed by a high degree of intermittency. This term, in statistics, denotes the occurrence of spiky events which are sporadic and burst-like. It may happen indeed, that non-linear interactions occasionally concur in such a way that responses of very large amplitudes are observed. Such statistical deviations are commonly referred to as extreme events. These instances cause higher-order moments to converge with greater difficulty, suggesting a significant departure from Gaussian statistics and hence non-homogeneous distribution of energy in time. In this paper, we aim to characterise, for the first time to the authors' knowledge, the intermittency of the wall-pressure signature in the separated region of an over-expanded TIC nozzle, experimentally tested at the PPRIME institute[10] at different NPR's and numerically reproduced by means of a delayed detached eddy simulation (DDES) at NPR = 9, which corresponds to the NPR of maximum aerodynamic side load.[10] The final goal is to find the basis for the formulation of a stochastic model capable of describing the intermittent behaviour of the aerodynamic loads.

2. Experimental and numerical test case

2.1 Experimental setup

The experimental campaign has been conducted in the S150 supersonic wind tunnel at PPRIME Institute. A rigid TIC nozzle, shown in figure 1, is considered with a divergent length $L = 0.1827$ m, a throat diameter $D_t = 0.038$ m and an exit diameter $D_e = 0.097$ m, which lead to a full-flowing flow condition with a Mach number $M = 3.5$. The nozzle is supplied with cold (total temperature around 260 K) and dry high-pressure air. The inflow stagnation pressure is varied in order to obtain nozzle pressure ratios in the range 6-12. The nozzle Reynolds number range, evaluated assuming the throat radius as the reference length, the total pressure p_0, the total temperature T_0 and the molecular viscosity taken at the stagnation-chamber condition $\mu_0 = \mu(T_0)$ is:

$$2.67 \cdot 10^6 \leq Re = \frac{\sqrt{\gamma}}{\mu_0} \frac{p_0 r_t}{\sqrt{R_{air} T_0}} \leq 5.34 \cdot 10^6. \tag{1}$$

The nozzle is equipped with 18 flush-mounted Kulite XCQ-062 pressure transducers, distributed along 3 rings of 6 transducers placed equidistantly along the circumference. Additional details on the experimental setup can be found in Jaunet et al.[10]

2.2 Numerical setup

The over-expanded jet has also been numerically reproduced by carrying out a DDES with an in-house code developed at Sapienza University of Rome, previously employed for similar flow cases.[6,16] Simulating the unsteady flow features of supersonic nozzle flows such as the one under consideration is particularly challenging: sufficiently high resolution is required both near the walls-to capture attached boundary layers-and further downstream, where unsteady turbulent structures develop. This results in very restrictive time steps, while long simulation times are necessary to capture the expected low-frequency and mid-frequency features of the integrated wall-pressure forces. For this reason, the DDES

DOI: 10.13009/EUCASS2025-130

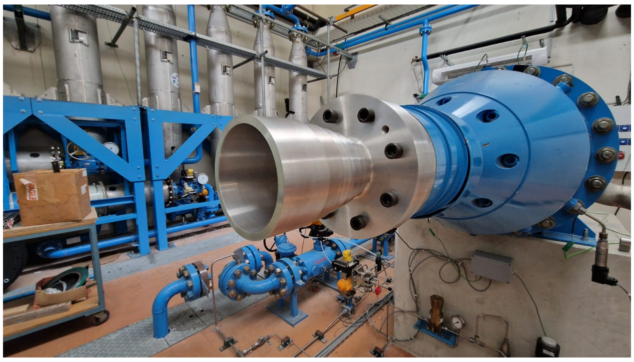

Figure 1: Experimental apparatus at PPRIME Institute.

method proposed by Spalart[19] has been adopted, as it enables effective resolution of the relevant scales of the separated flow while keeping the computational cost within practical limits.

We solve the three-dimensional Navier-Stokes equations for a compressible, viscous, heat-conducting gas

$$
\begin{aligned}
\frac{\partial \rho}{\partial t} + \frac{\partial(\rho\, u_j)}{\partial x_j} &= 0, \\
\frac{\partial(\rho\, u_i)}{\partial t} + \frac{\partial(\rho\, u_i u_j)}{\partial x_j} + \frac{\partial p}{\partial x_i} - \frac{\partial \tau_{ij}}{\partial x_j} &= 0, \\
\frac{\partial(\rho\, E)}{\partial t} + \frac{\partial(\rho\, E u_j + p u_j)}{\partial x_j} - \frac{\partial(\tau_{ij} u_i - q_j)}{\partial x_j} &= 0,
\end{aligned}
\tag{2}
$$

where ρ is the density, u_i is the velocity component in the i-th coordinate direction ($i = 1, 2, 3$), E is the total energy per unit mass, p is the thermodynamic static pressure. The total stress tensor τ_{ij} is the sum of the viscous and the Reynolds stress tensor,

$$
\tau_{ij} = 2\,\rho\,(\nu + \nu_t)\, S^*_{ij} \qquad S^*_{ij} = S_{ij} - \frac{1}{3}\, S_{kk}\, \delta_{ij}, \tag{3}
$$

where the Boussinesq hypothesis is applied through the introduction of the eddy viscosity ν_t, S_{ij} is the strain-rate tensor and ν the kinematic viscosity, depending on temperature T through Sutherland's law. Similarly, the total heat flux q_j is the sum of a molecular and a turbulent contribution

$$
q_j = -\rho\, c_p \left(\frac{\nu}{\mathrm{Pr}} + \frac{\nu_t}{\mathrm{Pr}_t} \right) \frac{\partial T}{\partial x_j}, \tag{4}
$$

where Pr and Pr_t are the molecular and turbulent Prandtl numbers, assumed to be 0.72 and 0.9, respectively.

2.2.1 Turbulence modelling

Because of the high-Reynolds numbers of the flow investigated in this work, the adopted numerical methodology is the DDES,[19] based on the Spalart-Allmaras (SA) turbulence model, which solves a transport equation for a pseudo eddy viscosity $\tilde{\nu}$:

$$
\frac{\partial(\rho\tilde{\nu})}{\partial t} + \frac{\partial(\rho\,\tilde{\nu}\, u_j)}{\partial x_j} = c_{b1}\tilde{S}\rho\tilde{\nu} + \frac{1}{\sigma}\left[\frac{\partial}{\partial x_j}\left[(\rho\nu + \rho\tilde{\nu})\, \frac{\partial \tilde{\nu}}{\partial x_j} \right] + c_{b2}\,\rho \left(\frac{\partial \tilde{\nu}}{\partial x_j} \right)^2 \right] - c_{w1} f_w \rho \left(\frac{\tilde{\nu}}{\tilde{d}} \right)^2, \tag{5}
$$

where $\tilde{d}$ is the model length scale, f_w is a near-wall damping function, $\tilde{S}$ a modified vorticity magnitude, and σ, c_{b1}, c_{b2}, c_{w1} model constants. The eddy viscosity in Eq. 3 is related to $\tilde{\nu}$ through $\nu_t = \tilde{\nu}\, f_{v1}$, where f_{v1} is a correction function designed to guarantee the correct boundary-layer behaviour in the near-wall region. The destruction term in Eq. 5 is built in such a way that the model reduces to pure RANS in attached boundary layers and to a LES sub-grid scale model in separated flow regions. This task is accomplished by defining the length-scale $\tilde{d}$ as

$$
\tilde{d} = d_w - f_d \max\left(0, d_w - C_{DES}\, \Delta\right), \tag{6}
$$

where d_w is the distance from the nearest wall, Δ is the subgrid length-scale that controls the wavelengths resolved in LES mode and C_{DES} is a calibration constant equal to 0.20. The function f_d, designed to be 0 in boundary layers and

DOI: 10.13009/EUCASS2025-130

1 in LES regions, is defined as

$$f_d = 1 - \tanh\left[(16 r_d)^3\right], \qquad r_d = \frac{\tilde{\nu}}{k^2\, d_w^2\, \sqrt{U_{i,j} U_{i,j}}}, \tag{7}$$

where $U_{i,j}$ is the velocity gradient and k the von Karman constant. The introduction of f_d guarantees that the boundary layer is modeled in RANS mode also in the presence of particularly fine grids, for which the spacing in the wall-parallel directions does not exceed the boundary layer thickness. This precaution is needed to prevent the phenomenon of model stress depletion.[7] The sub-grid length scale in this work is defined according to Deck,[7] and it depends on the flow itself, through f_d as

$$\Delta = \frac{1}{2}\left[\left(1 + \frac{f_d - f_{d0}}{|f_d - f_{d0}|}\right)\Delta_{\max} + \left(1 - \frac{f_d - f_{d0}}{|f_d - f_{d0}|}\right)\Delta_{\mathrm{vol}}\right], \tag{8}$$

where $f_{d0} = 0.8$, $\Delta_{\max} = \max(\Delta x, \Delta y, \Delta z)$ and $\Delta_{\mathrm{vol}} = (\Delta x \cdot \Delta y \cdot \Delta z)^{1/3}$. The main idea of this formulation is to take advantage of the f_d function to switch between Δ_{max}, needed to shield the boundary layer, and Δ_{vol}, needed to ensure a rapid destruction of modelled viscosity and trigger the formation of turbulent structures.

The computational domain includes the nozzle and an extended portion of the external ambient. The total pressure, total temperature, and flow direction are imposed at the nozzle inflow, while an assigned ambient pressure p_a is prescribed at the outer boundaries. The nozzle walls are treated with a no-slip adiabatic boundary condition. The final grid consists of approximately 115 million cells, including 260 cells in the azimuthal direction. The mesh resolution and total number of cells are based on previous similar simulations.[6,16]

3. Flow field organization and spectral characterization

Figure 2 shows an instantaneous numerical Schlieren image in a longitudinal view, illustrating an enlarged visualization of the flow topology under consideration. First, the separation-induced converging conical shock is observed, which reflects as a Mach disk on the nozzle centreline, followed by a diverging conical shock originating from the triple point. Two supersonic shear layers are also evident: the outer one separates the wall-detached supersonic jet from the subsonic recirculating air entrained from the ambient; the inner shear layer, emanating from the triple point, separates the detached supersonic jet from the subsonic region downstream of the Mach disk. Both shear layers impinge on the second Mach disk, located just downstream of the nozzle exit.

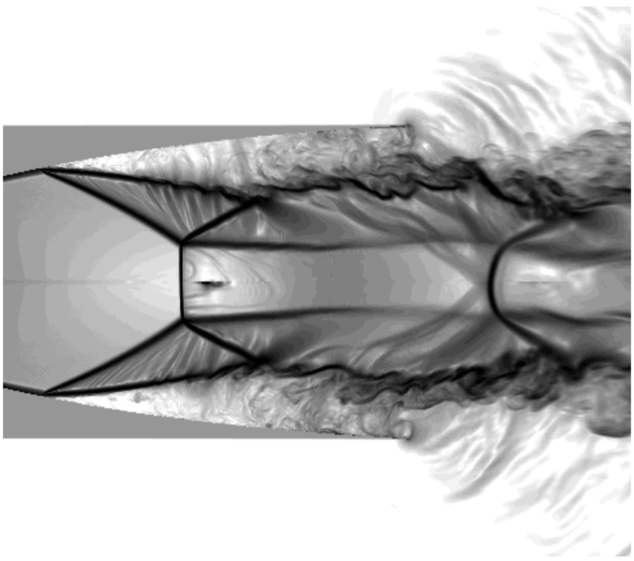

Figure 2: Instantaneous visualisation of the turbulent and shock structures at NPR=9 from DDES: numerical Schlieren on a longitudinal view.

In the following we present the spectral characterization of the experimental and numerical wall-pressure signals. The power spectral density (PSD) of the pressure fluctuations is defined as the Fourier transform of their auto-correlation function:

DOI: 10.13009/EUCASS2025-130

$$< p_w p_w^* > (\omega) = \int_{-\infty}^{\infty} < p_w(t) p_w^*(t+\tau) > e^{-i\omega\tau} d\tau, \tag{9}$$

where $< \cdot >$ is the average operator, $\omega = 2\pi f$ is the pulsation and the asterisk indicates the complex conjugation. The PSD of the experimental wall-pressure signal extracted at $x/L = 0.85$, $x/L = 0$ being the nozzle throat, is reported in figure 3 (left) together with the spectrum of the numerical signal. As we already know from literature,[2] we recognize two peak frequencies at $\approx$ 2000Hz and $\approx$ 3000Hz, which are correctly reproduced by the simulation. These two frequencies are associated with the first and the second azimuthal modes, as we shall see in the following.

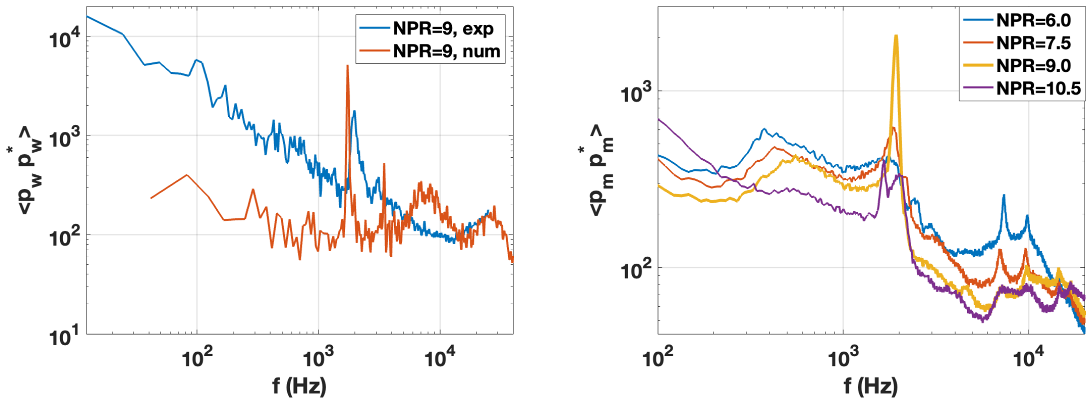

Figure 3: Left) PSD's of the experimental and numerical wall-pressure signals at $x/L = 0.67$ for $NPR = 9$. Right) Experimental PSD's of the first pressure azimuthal mode as a function of frequency at $x/L = 0.67$ for $NPR = 6, 7.5, 9, 10.5$.

Our focus is directed on the first pressure azimuthal mode, since it is the only responsible of the aerodynamic side loads. Therefore, the wall-pressure signals along all the nozzle are decomposed into the azimuthal modes:

$$p_{w,m}(x,t) = \int_0^{2\pi} p_w(x,\theta,t) e^{im\theta} d\theta \tag{10}$$

with the first three modes $m = 0$, $m = 1$ and $m = 2$ indicating the breathing (symmetric), the helical (asymmetric) and the ovalization modes, respectively. Figure 3 (right) shows the power spectral densities of the asymmetric mode ($m = 1$) of the experimental signals extracted at $x/L = 0.67$ for $NPR = 6, 7.5, 9, 10.5$. It is evident that the PSDs of all the NPRs, except the first case, are characterized by remarkable peaks with frequencies ranging approximately from 1700 Hz to 2000 Hz, with a predominance of the peak at $NPR = 9$. We know from literature that these peaks are coherent all along the nozzle wall where flow-separation occurs.[10]

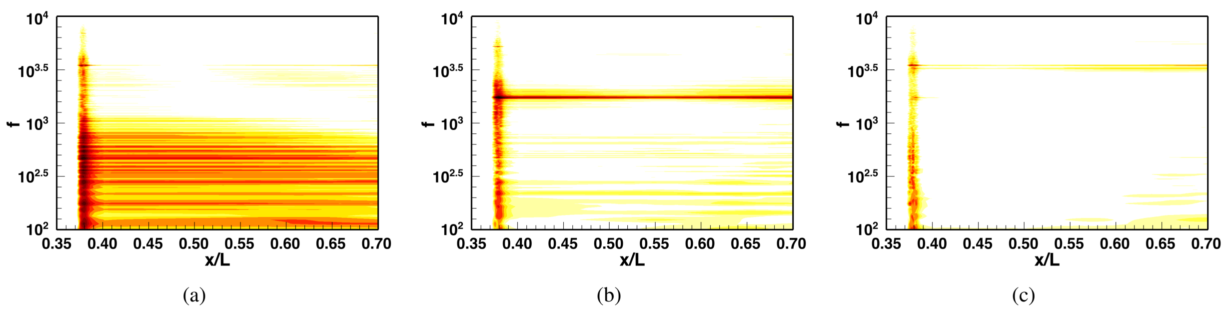

Figure 4: Numerical PSD maps of the wall-pressure signals along the nozzle for the first three azimuthal modes at $NPR = 9$: (left) $m = 0$, (centre) $m = 1$, (right) $m = 2$.

The DDES simulation of the test case at $NPR = 9$ confirms this important result. Figure 4, from left to right, shows the numerical PSD maps for the breathing, helical and ovalization modes all along the nozzle wall. It is evident from this figure that the region corresponding to the separation point ($x/L \approx 0.38$) is characterized by fluctuation energy spread over a wide range of frequencies, whereas downstream each azimuthal mode is dominated by a particular

DOI: 10.13009/EUCASS2025-130

temporal frequency, in good correspondence with the experimental peak-frequencies. Moreover, the signature of the breathing, helical and ovalization modes persists all along the separated region confirming the observations of Jaunet et al.[10] and Morisco et al.:[21] this observation suggests that the whole jet column, at least the part inside the nozzle, is subject to unsteadiness at these frequencies.

4. Wavelet analysis of intermittency

Similarly to the approach adopted in Bernardini et al.,[3] the wavelet transform is here applied to extract energetic intermittent events. Indeed, this approach allows for the extraction of local (in time) features that may be partially lost using Fourier analysis, thanks to the projection on a set of basis functions characterized by a compact support in both the physical and the frequency space.[22] The wavelet transform is computed by the convolution of the wall-pressure signal $p_w(t)$ with the dilated (by the factor k) and translated (by the factor t) complex conjugate counterpart of a so-called mother wavelet, according to the following formalism:

$$w_\Psi(k,t) = \frac{1}{\sqrt{k}} \int_{-\infty}^{+\infty} p_w(\tau)\Psi^*\left(\frac{\tau - t}{k}\right) \mathrm{d}\tau \,, \tag{11}$$

where Ψ is the wavelet mother function, k is a dilatation parameter indicating the time scale of the event under consideration, t is the time-translation parameter. A detailed theoretical framework can be found in Farge[9] and Mallat.[15] In this study, the Morlet wavelet has been chosen, as a higher resolution in frequency can be achieved compared to other mother functions.

The wavelet scalograms of the experimental and numerical wall-pressure signals extracted at $x/L = 0.67$ are reported in figure 5 (top left and right) for a segment of 0.1 s. It must be noted that the total time of analysis for the experimental test case is 20 s whereas the total integration time for the DDES is 0.11s due to the relevant computational resources required (despite the use of a hybrid RANS/LES method). Nevertheless, it is evident that the numerical simulation adequately reproduces the qualitative time distribution of the events. We now focus on the frequency ranges corresponding to $m = 1$, that is around 2000 Hz: it is evident that the wavelet decomposition highlights that the temporal evolution of the energy at these frequencies is strongly intermittent, since burst of high energy are alternated to period of relatively low energy levels.

As previously observed, the qualitative aspects of the scalogram are very similar to the compressible-jet acoustic data in the time-frequency domain presented in Camussi et al.,[5] which thus seems to suggest a common characteristics to all jets. Once computed the wavelet transform coefficients $w_\Psi(k,t)$, it is possible to obtain the scale-time distribution of the energy density $|w_\Psi(k,t)|^2$ of the wall-pressure signal. Thanks to this property, an effective indicator of the intermittency is the squared local intermittency measure, denoted as $LIM2$:[4]

$$LIM2(k,\tau) = \frac{|w_\Psi(k,t)|^4}{\langle |w_\Psi(k,t)|^2 \rangle_t^2} \,. \tag{12}$$

where $\langle \bullet \rangle_t$ indicates the time average of the considered quantity. $LIM2$ can be interpreted as a time-scale dependent measure of the flatness factor or kurtosis of wall-pressure signals. Therefore, the $LIM2$ parameter will be equal to 3 when the probability distribution is Gaussian, while the condition $LIM2 > 3$ identifies only those rare bursts of energy contributing to the deviation of the wavelet coefficients from a normal, Gaussian distribution. The $LIM2$ maps are reported in figure 5 for the experimental signal (bottom left) and the numerical signal (bottom right) and we can individuate the bursts of energies which induce a non-homogeneous distribution in time. The events characterised by large temporal scales (low-frequencies) are very rare, but also the events with the temporal scale (or frequency) linked to the $m = 1$ mode are rather sparse with respect to the turbulent events (highest frequency range).

Following the literature,[4] we investigate intermittency by evaluating the delay time Δt between the various energetic events. We will focus our attention only on the events in the frequency range of the $m = 1$ mode, since we want to characterize the aerodynamic loads given by the non-symmetrical azimuthal mode. It should be noted that this intermittency is not related to the fluid dynamics concept of turbulence intermittency.[13] Lacking a well-defined theoretical basis, an ad hoc definition of an *"event"* is necessary and we mimic the methodology developed by Camussi et al.[4] based on the inspection of the LIM2 map. Therefore, we compute the delay times with the following tracking procedure:

1. extraction of the LIM2 values corresponding to a scalogram region where $m = 1$ dominates: $1000Hz < f < 2800Hz$, and average of the values in the selected frequency range. The resulting time signal is shown in figure 6;

2. selection of times t_i of the events with $LIM2 > \sigma_{LIM2}$, where σ_{LIM2} is the standard deviation of the extracted LIM2 values;

DOI: 10.13009/EUCASS2025-130

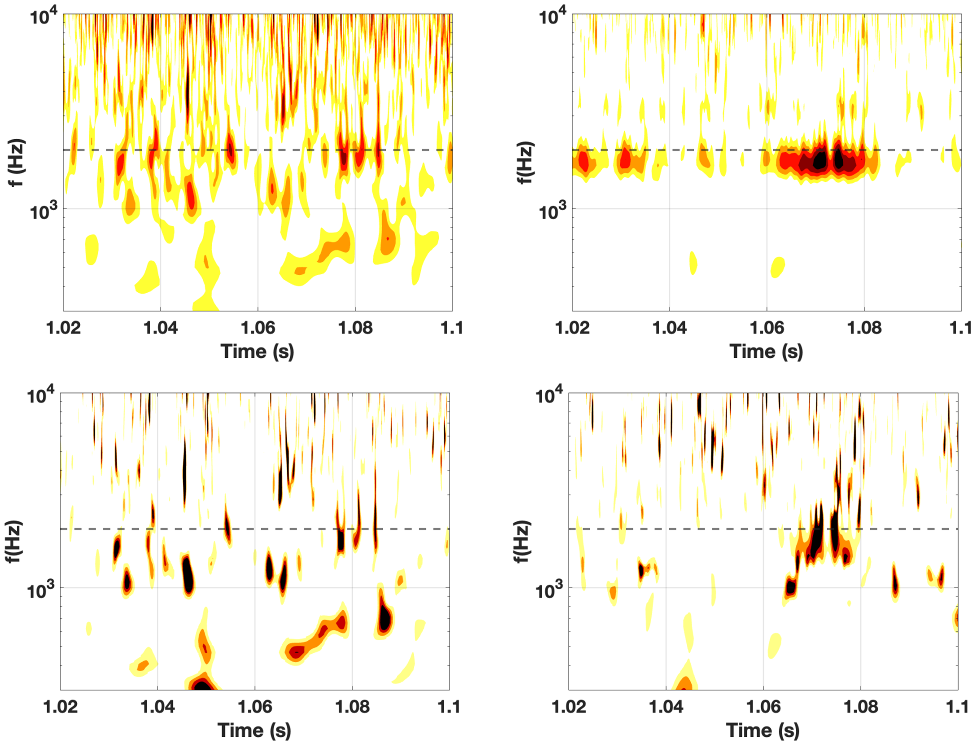

Figure 5: Scalograms of the experimental (top left) and numerical (top right) wall-pressure signals at $x/L = 0.67$ for $NPR = 9$. The grey dashed lines indicate the characteristic frequency of the $m = 1$ mode; bottom left) LIM2 map of the experimental wall-pressure signal at $x/L = 0.67$ for $NPR = 9$; bottom right) LIM2 map of the numerical wall-pressure signal at $x/L = 0.67$ for $NPR = 9$. The LIM2 maps only show values greater than 3.

3. evaluation of $\Delta t_{m=1}(i) = t_{i+1} - t_i$;
4. local average of the wavelet power spectrum w^2 in the selected range of frequencies. Evaluation of $w_i^2 = [w_i(t_i)]^2$ from the obtained time distribution.

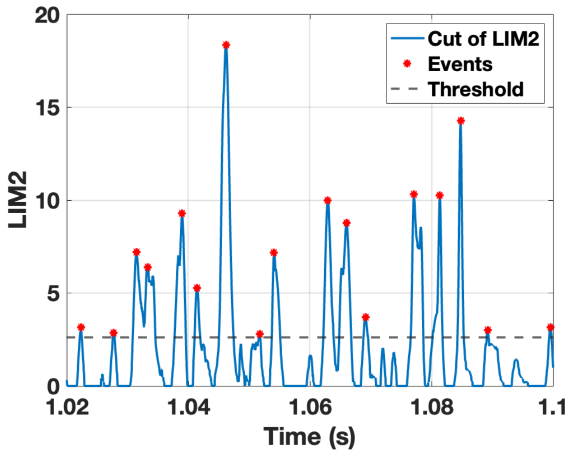

Figure 6: Procedure for the selection of the events in the LIM2 map.

5. Statistic analysis of events

The purpose of this section is to investigate the nature of the extracted quantities through statistical analysis, in order to determine how these quantities scale with the NPR and the distance from the separation location.

DOI: 10.13009/EUCASS2025-130

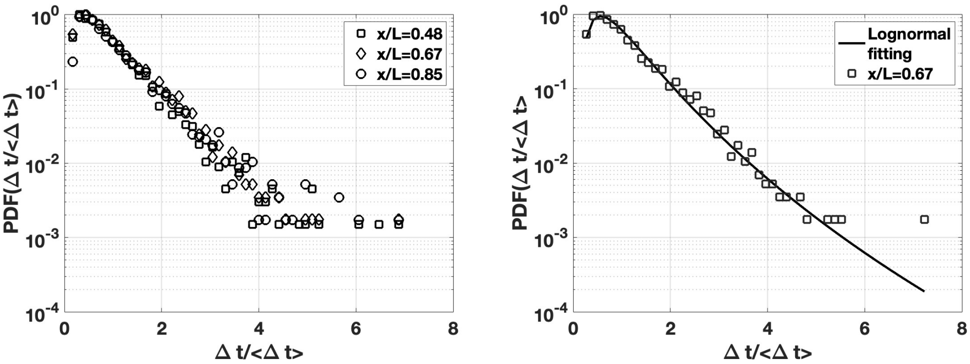

Figure 7: Left) PDF of the delay times between events at $NPR = 9$ for the azimuthal mode m_1 for different distances from the separation location; right) lognormal fit for the delay time PDF evaluated at $x/L = 0.67$.

5.1 Intermittency: time between events.

The probability density functions (PDFs) of the extracted time delays, normalized by their average value ($\Delta t / < \Delta t >$) at $x/L = 0.48, 0.67, 0.85$ are shown in figure 7 (left) for $NPR = 9$. First of all, it appears that these distributions share the same statistical behaviour from a quantitative point of view, indicating a global behaviour of the jet column, at least inside the nozzle. The distribution of the time delays at $x/L = 0.67$ is then fit with a log-normal distribution in figure 7 (right) since it resulted to be the best approximation among different trials. It could be useful to remember that the log-normal distribution emerges naturally in contexts where times or phenomena are the result of multiplicative rather than additive processes.[12] This kind of distribution has a strong skewness and a long right tail, indicating a significant variability in the time intervals. Physically, this may reflect a system in which the probability of a long interval is not negligible. The obtained results are in line with the findings of Camussi et al.[5] about the waiting times of the noise-emitting events in the near field (hydrodynamic pressure) of two compressible subsonic jets at $M_{jet} = 0.6$ and $M_{jet} = 0.9$. Kearney et al.,[13] instead, investigated the noise-emitting events in the far field (acoustic pressure) of a data set of compressible subsonic jet, with jet Mach number ranging from 0.5 to 0.9, and they have found the best fitting for the time delays to be a *gamma* distribution. This kind of distribution arises from processes that are of additive nature and the occurrences of the events are independent of each other.

The peak frequencies of the first azimuthal modes for all the other NPRs, as shown in figure 3, are included in the same interval for the averaging procedure around $f_{m=1}$ used for the selection of the events at $NPR = 9$. The analysis of the PDFs of the time delays along the nozzle wall for all the NPRs reveals a behaviour very similar to the case at $NPR = 9$, as shown in figure 8. All the distributions indeed are almost independent of the location along the nozzle. Even if the aerodynamic load presents a maximum at $NPR = 9$,[10] there is not a qualitative effect of the nozzle pressure ratio on the distribution of the time delays.

The behaviour of the mean delay time $< \Delta t >$ and the standard deviation $\sigma_{\Delta t}$ along the nozzle wall are reported in figure 9 (top left and right). It appears that there is only a very slight effect of NPR and x/L. This figure reports also the mean delay times and the standard deviations of Δt evaluated from DDES, since these are the only statistical quantities that we can evaluate, given the limited integration time. It is evident that the values extracted from the numerical analysis are of the same order of magnitude of the experimental values and they show a similar qualitative behaviour moving along the nozzle wall. The best-fit log-normal parameters $\mu_{\Delta t/<\Delta t>}$ (location) and $\nu_{\Delta t/<\Delta t>}$ (shape) are reported in figures 9 (bottom left and right), whereas all the values of the statistical characterization are reported in table 1. Again, it appears that there is not a clear trend varying the NPR and the location along the nozzle x/L.

The PDFs for all the 12 cases are shown in figure 10. Additionally, a unique fitting distribution curve based on the averaged log-normal parameters ($\mu_{\Delta t,av} = -021088$ and $\nu_{\Delta t,av} = 0.6349$) is shown as a black solid line. Although the collapse is not quite good at high values of $\Delta t / < \Delta t >$, it seems sufficient to say that the mean event delay time is the controlling parameter of the distribution. Once the mean value is known, the entire distribution can be reasonably well predicted based on the global values $\mu_{\Delta t,av} = -0.21088$ and $\nu_{\Delta t,av} = 0.6349$.

5.2 Event energy distribution

A similar approach has been adopted for the stochastic modelling of the amplitude of the intermittent events. The PDFs of the selected-events' energy, indicated by the square of the wavelet coefficients and normalized by their avarage value, $w^2 / < w^2 >$, are presented in figure 11 for all the NPR's analysed. It now appears that there is an effect of the location

DOI: 10.13009/EUCASS2025-130

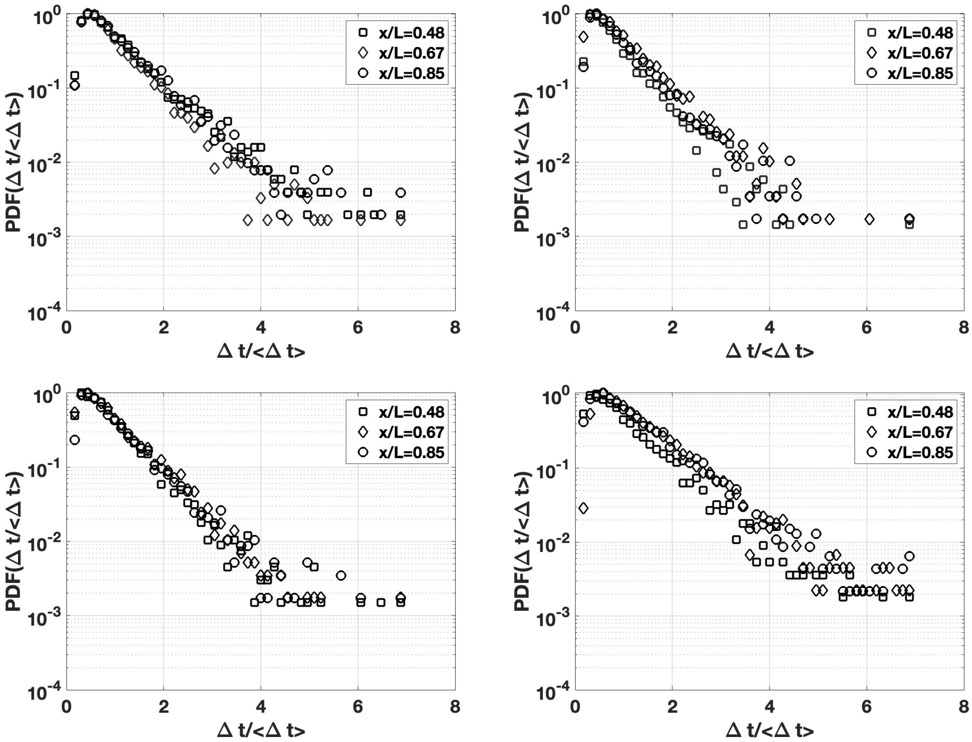

Figure 8: PDF of the delay times between events for the azimuthal mode m_1 for different distances from the separation location at top left) $NPR = 6$; top right) $NPR = 7.5$; bottom left) $NPR = 9$; bottom right) $NPR = 10.5$.

NPR	x/L	$<\Delta t>, s$	$\sigma_{\Delta t}, s$	$\mu_{\Delta t}$	$\nu_{\Delta t}$
6.0	0.48	0.0054	0.0042	-0.227	0.659
6.0	0.67	0.0051	0.0037	-0.207	0.629
6.0	0.85	0.0053	0.0039	-0.216	0.647
7.5	0.48	0.0053	0.00402	-0.225	0.656
7.5	0.67	0.0047	0.00322	-0.190	0.608
7.5	0.85	0.0056	0.00422	-0.226	0.659
9.0	0.48	0.0045	0.00313	-0.190	0.605
9.0	0.67	0.0049	0.00338	-0.196	0.619
9.0	0.85	0.0054	0.00416	-0.234	0.676
10.5	0.48	0.0048	0.00341	-0.204	0.627
10.5	0.67	0.005	0.00348	-0.199	0.625
10.5	0.85	0.0046	0.00315	-0.190	0.609

Table 1: Parameters characterizing the log-normal PDF of the delay time Δt.

along the nozzle and an effect of the NPR. Figure 12 (top left and right) shows that both the average amplitude $< w^2 >$ and standard deviation σ_{w^2} are almost independent from the distance and the NPR, with the relevant exception of the case $NPR = 10.5$ at $x/L = 0.48$. This is reasonably due to the fact that at this NPR the pressure sensor is really close to the separation shock, therefore it is alternately subject to the pressure of the attached and separated boundary layer. The best fit resulted again to be the log-normal distribution. The fitting parameters, $\mu_{w^2/<w^2>}$ and $\nu_{w^2/<w^2>}$, are reported in figure 12 (bottom left and right) as function of the distance from the separation line and of the NPR, whereas their numerical values are summarized in table 2.

It is clear that the whole picture is more complex. It is possible to see that both the location μ_{w^2} and shape ν_{w^2} are influenced by the NPR and the distance x/L. In particular, while for NPR=6 and 7 the parameters are more similar to each other and along the nozzle wall, for NPR=9 μ_{w^2} decreases significantly with x/L and ν_{w^2} increases. The opposite occurs for $NPR = 10.5$. This general non-monotonic behaviour could be attributed to the particular

DOI: 10.13009/EUCASS2025-130

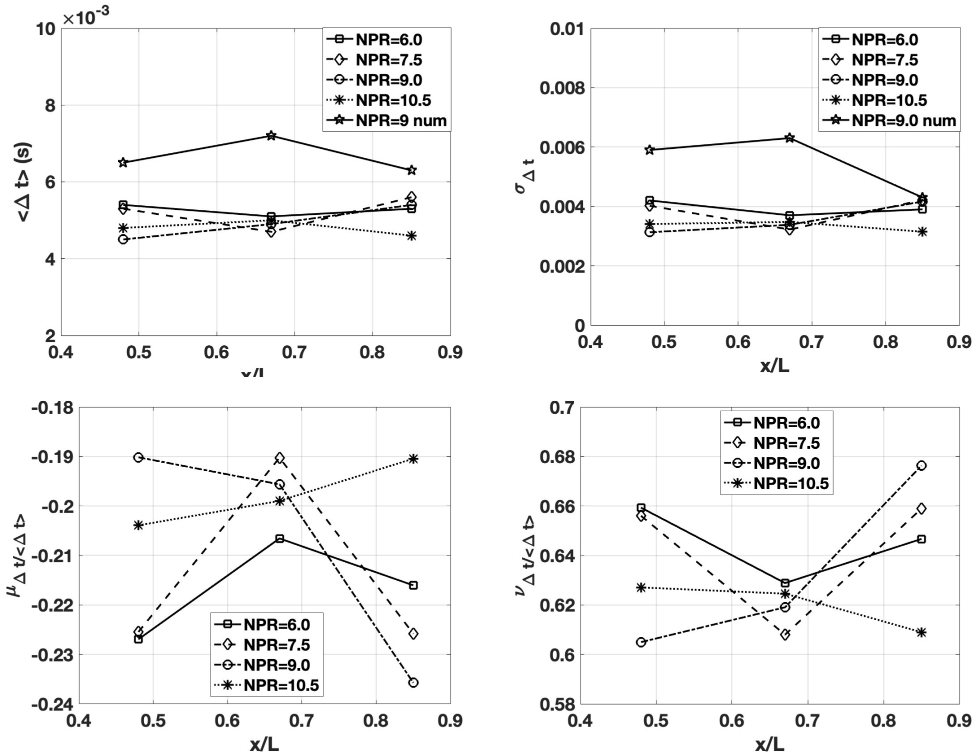

Figure 9: Comparison of $< \Delta t >$ (top left), of $\sigma_{\Delta t}$ (top right), of the log-normal PDF parameters $\mu_{\Delta_t/<\Delta t>}$ (bottom left) and $\nu_{\Delta_t/<\Delta t>}$ (bottom right) for the different locations along the nozzle wall and for all the NPR's.

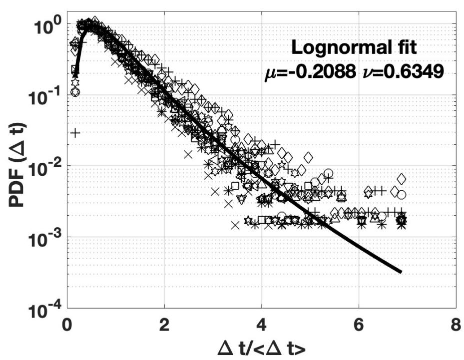

Figure 10: Intermittence distributions for all the NPR's and locations along the nozzle wall together with the proposed universal lognormal fit.

aerodynamic transverse-load distribution along the nozzle wall, as shown in Bakulu et al.:[2] the trend along the nozzle wall is non-monotonic, with a peak immediately downstream of the separation shock ($x/L \approx 0.5$) and then two bumps downstream for $x/L \approx 0.65$ and $x/L \approx 0.95$. To increase the complexity of the phenomenon, one could also consider the fact that the sensors are not located at equal distances from the jet, and that the growth rate of the Kelvin-Helmotz instability of the detached shear layer might also influece the evolution of these events. Based on the currently available data, the only firm conclusion we can draw is that energy, like intermittency, also follows a log-normal distribution, thereby suggesting a phenomenology driven by multiplicative rather than additive factors.

6. Conclusions

This work presents a combined experimental and numerical investigation into the unsteady dynamics of wall-pressure fluctuations in a supersonic over-expanded nozzle with free shock separation, with a specific focus on the statistical characterization of intermittent events associated with the first azimuthal mode. It is observed that this mode is charac-

DOI: 10.13009/EUCASS2025-130

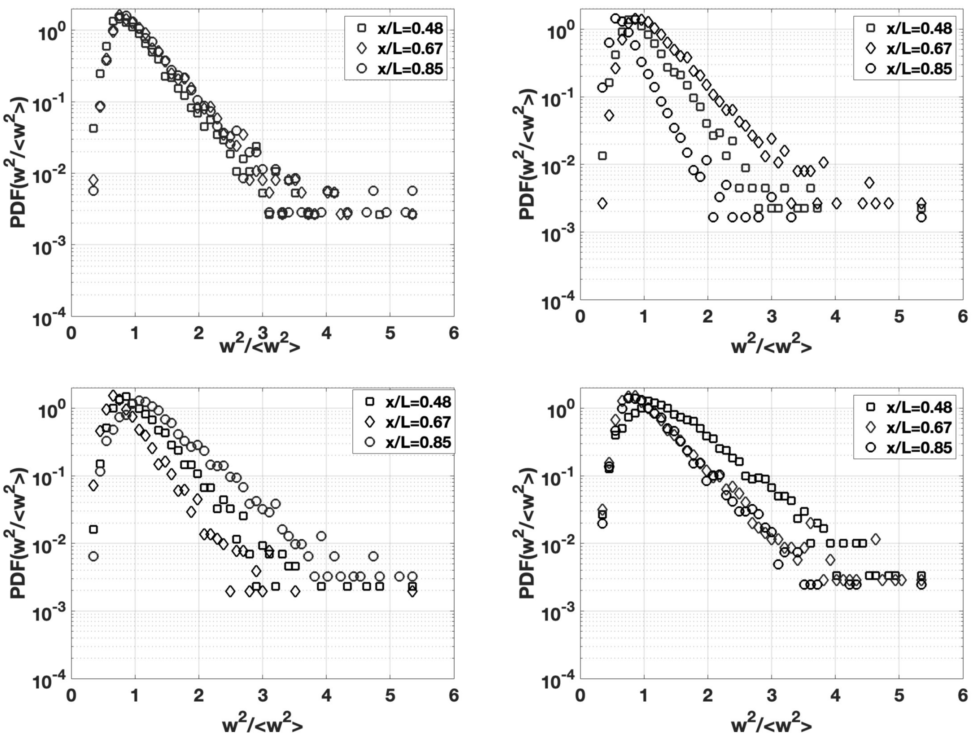

Figure 11: PDF of the energy $w^2/<w^2>$ for the azimuthal mode m_1 for different distances from the separation location at top left) $NPR = 6$; top right) $NPR = 7.5$; bottom left) $NPR = 9$; bottom right) $NPR = 10.5$.

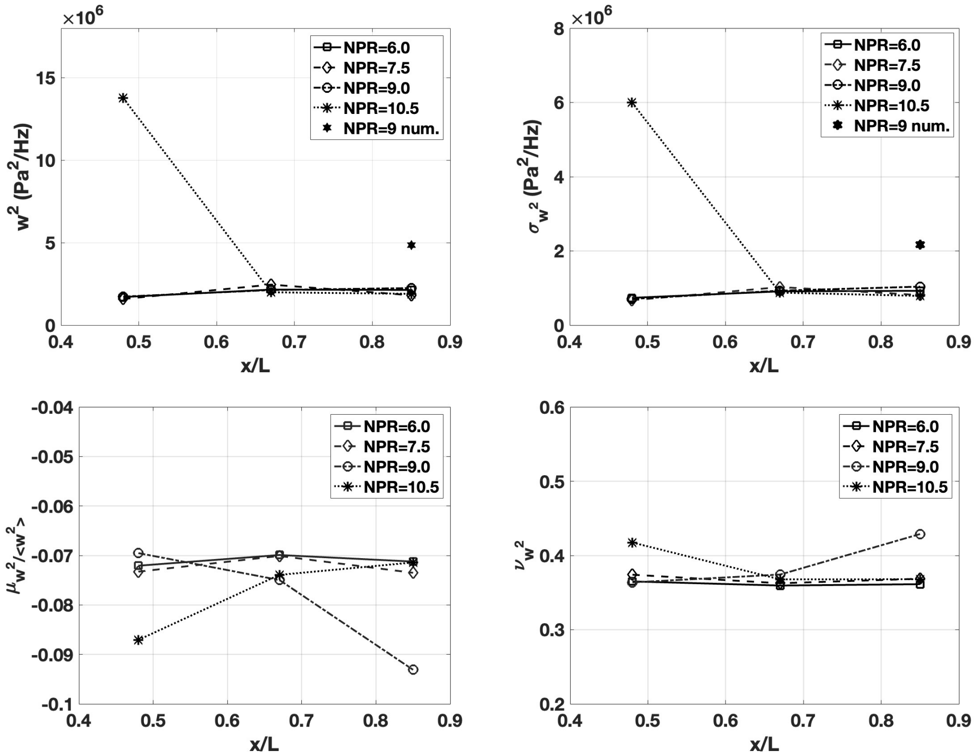

Figure 12: Comparison of $< w^2 >$ (top left), of σ_{w^2} (top right), of the log-normal PDF parameters $\mu_{w^2/<w^2>}$ (bottom left) and $\nu_{w^2/<w^2>}$ (bottom right) for the different locations along the nozzle wall and for all the NPR's.

terized by localized, sparse bursts of energy, referred to as intermittent events. The statistics of these events have been

DOI: 10.13009/EUCASS2025-130

NPR	x/L	$< w^2 >, Pa^2/Hz$	$\sigma_{w^2}, Pa^2/Hz$	μ_{w^2}	ν_{w^2}
6	0.48	$1.7 \cdot 10^6$	$7.4 \cdot 10^5$	-0.0720734	0.3650
6	0.67	$2.2 \cdot 10^6$	$9.1 \cdot 10^5$	-0.0699088	0.3595
6	0.85	$2.1 \cdot 10^6$	$9.3 \cdot 10^5$	-0.0712341	0.361321
7.5	0.48	$1.6 \cdot 10^6$	$6.7 \cdot 10^5$	-0.0732723	0.374054
7.5	0.67	$2.5 \cdot 10^6$	$1.0 \cdot 10^5$	-0.0700999	0.362572
7.5	0.85	$1.8 \cdot 10^6$	$8.1 \cdot 10^5$	-0.0735011	0.368633
9.0	0.48	$1.7 \cdot 10^6$	$7.1 \cdot 10^5$	-0.0695205	0.363713
9.0	0.67	$2.1 \cdot 10^6$	$9.3 \cdot 10^5$	-0.074962	0.37429
9.0	0.85	$2.2 \cdot 10^6$	$1.0 \cdot 10^6$	-0.0931035	0.42883
10.5	0.48	$1.4 \cdot 10^6$	$6.0 \cdot 10^5$	-0.0870711	0.417416
10.5	0.67	$2.0 \cdot 10^6$	$8.8 \cdot 10^5$	-0.0739211	0.367807
10.5	0.85	$1.9 \cdot 10^6$	$7.9 \cdot 10^5$	-0.0714131	0.36794

Table 2: Parameters characterizing the lognormal PDF of the amplitude w^2.

analysed by selecting energetic occurrences from the wavelet scalogram within the frequency range associated with the first azimuthal mode for various NPR values. These selected events are used to extract two key random variables: the time interval between successive bursts, Δt, and the amplitude of their energy content, w^2. The statistical analysis of these two variables reveals that both follow a log-normal distribution. Moreover, the probability density function (PDF) of the time intervals appears to exhibit a universal behaviour, whereas the PDF of the amplitude depends on both the NPR and the sensor location along the nozzle wall. These statistical properties may provide a foundation for the development of stochastic models capable of reproducing aerodynamic side loads in configurations where the nozzle exhibits free shock separation.

7. Acknowledgments

The simulation has been performed thanks to computational resources provided by the Cineca Italian Computing Center under the Italian Super Computing Resource Allocation initiative (ISCRA B/DESNON/HP10BLZA22).

References

[1] Woutjin J. Baars, Charles E. Tinney, Joseph H. Ruf, Andrew M. Brown, and David M. McDaniels. Wall pressure unsteadiness and side loads in overexpanded rocket nozzles. *AIAA Journal*, 50(1):61–73, 2012.

[2] Florian Bakulu, Guillaume Lehnasch, Vincent Jaunet, Eric Goncalves da Silva, and Steve Girard. Jet resonance in truncated ideally contoured nozzles. *Journal of Fluid Mechanics*, 919:A32, 2021.

[3] M. Bernardini, G. Della Posta, F. Salvadore, and E. Martelli. Unsteadiness characterisation of shock wave/turbulent boundary-layer interaction at moderate Reynolds number. *J. Fluid Mech.*, 954:A43, 2023.

[4] R. Camussi and C. Bogey. Intermittent statistics of the 0-mode pressure fluctuations in the near field of mach 0.9 circular jets at low and high reynolds numbers. *Theor. Comput. Fluid Dyn.*, 35:229–247, 2021.

[5] R. Camussi, A. Di Marco, and T. Castelain. Statistical analysis of the hydrodynamic pressure in the near field of compressible jets. *International Journal of Heat and Fluid Flow*, 64:1–9, 2017.

[6] M. Cimini, E. Martelli, and M. Bernardini. Numerical analysis of side-loads reduction in a sub-scale dual-bell rocket nozzle. *Flow Turbulence Combust*, 107:551–574, 2021.

[7] S. Deck. Recent improvements in the zonal detached eddy simulation (ZDES) formulation. *Theor. Comput. Fluid Dyn.*, 26:523–550, 2012.

[8] G. E. Dumnov. Unsteady side-loads acting on the nozzle with developed separation zone. In *32nd AIAA/ASME/SAE/ASEE Joint Propulsion Conference and Exhibit*, pages 1–8, 1996.

[9] M. Farge. Wavelet transforms and their applications to turbulence. *Annu. Rev. Fluid Mech.*, 24(1):395–458, 1992.

DOI: 10.13009/EUCASS2025-130

[10] V. Jaunet, S. Arbos, G. Lehnasch, and S. Girard. Wall pressure and external velocity field relation in overexpanded supersonic jets. *AIAA Journal*, 55(12):4245–4257, 2017.

[11] Vincent Jaunet and Guillaume Lehnasch. Linear dynamics of over-expanded annular supersonic jets. *Journal of Fluid Mechanics*, 1009:A32, 2025.

[12] Norman L. Johnson, Samuel Kotz, and N. Balakrishnan. *Continuous Univariate Distributions, Volume 1*. Wiley-Interscience, 2 edition, 1994.

[13] M. Kearney-Fischer, A. Sinha, and M. Samimy. Intermittent nature of subsonic jet noise. *AIAA Journal*, 51(5):1142–1155, 2013.

[14] Ching Y. Loh and K. B. M. Q. Zaman. Numerical investigation of transonic resonance with a convergent-divergent nozzle. *AIAA Journal*, 40(12):2393–2401, 2002.

[15] S. Mallat. *A wavelet tour of signal processing*. Elsevier, 1999.

[16] E. Martelli, L. Saccoccio, P. P. Ciottoli, C. E. Tinney, W. J. Baars, and M. Bernardini. Flow dynamics and wall-pressure signatures in a high-reynolds-number overexpanded nozzle with free shock separation. *Journal of Fluid Mechanics*, 895:A29, 2020.

[17] L. H. Nave and G. A. Coffey. Sea level side loads in high-area-ratio rocket engines. 1973.

[18] R. H. Schmucker. Flow process in overexpanded chemical rocket nozzles, part 2: Side loads due to asymmetric separation. Technical Memorandum TM-77395, NASA, 1984.

[19] P.R. Spalart, S. Deck, M.L. Shur, K.D. Squires, M.Kh. Strelets, and A.K. Travin. A new version of detached-eddy simulation, resistant to ambiguous grid densities. *Theor. Comput. Fluid Dyn.*, 20:181–195, 2006.

[20] Christopher K. W. Tam and Fang Q. Hu. On the three families of instability waves of high-speed jets. *Journal of Fluid Mechanics*, 201:447â483, 1989.

[21] C. Tarsia Morisco, J.-C. Robinet, J. Herpe, and D. Saucereau. Impinging shear layer instability in over-expanded nozzle dynamics. *Physics of Fluids*, 35(11):116118, 11 2023.

[22] Christopher Torrence and Gilbert P. Compo. A practical guide to wavelet analysis. *Bulletin of the American Meteorological Society*, 79(1):61 – 78, 1998.